Biosensors and Bioelectronics 180 (2021) 113090

Contents lists available at ScienceDirect

Biosensors and Bioelectronics

journal homepage: http://www.elsevier.com/locate/bios

Laser-etched grooves for rapid fluid delivery for a paper-based chemiresistive biosensor

Sidharth Modha [a,1], Yu Shen [b,1], Hussein Chamouni [c], Ashok Mulchandani [b,d], Hideaki Tsutsui [a,c,e,*]

[a] Department of Bioengineering, University of California, Riverside, Riverside, CA, 92521, USA
[b] Department of Chemical and Environmental Engineering, University of California, Riverside, Riverside, CA, 92521, USA
[c] Department of Mechanical Engineering, University of California, Riverside, Riverside, CA, 92521, USA
[d] Center for Environmental Research and Technology (CE-CERT), University of California, Riverside, Riverside, CA, 92507, USA
[e] Stem Cell Center, University of California, Riverside, Riverside, CA, 92521, USA

ARTICLE INFO

Keywords:
Paper-based microfluidics
Laser-etching
Groove
Wicking speeds
Flow control
Chemiresistive sensor

ABSTRACT

Paper-based microfluidic devices are an attractive option for developing low-cost, point-of-care diagnostic tools. To incorporate more complex assays into paper, these devices must become more sophisticated, through the sequential delivery of different liquids or reagents without user intervention. Many flow control strategies focus on slowing the fluid down. However, this can lead to increased assay times and sample loss due to evaporation. We report the use of a CO_2 laser to create etched grooves on paper to accelerate wicking speeds in paper-based microfluidic devices. We explored different laser settings to determine the optimal configuration. Our findings showed that simply cutting a slit into the paper created the fastest wicking channels. The slit acted as a macro capillary, allowing fluid to bypass the paper and speed it up. Further studies determined an ideal groove pitch of 0.75 mm (spacing in between grooves) for a paper channel. Additional experiments documented how sealing grooved channels with different adhesives can influence wicking. Overall, sealing the channels with tape made them wick faster. However, sealing methods such as lamination had a negative effect on wicking. Laser-etched grooves were successfully used to design a fluid-handling architecture for a chemiresistive paper-based biosensor. The grooves facilitated rapid, sequential delivery of sample and wash buffer. Human serum albumin spiked in phosphate buffer, artificial urine, and artificial saliva was successfully detected at as low as 15 pM. Etching grooves in paper is a simple process that requires no additional materials or chemicals, allowing single-step fabrication of paper-based microfluidic channels.

1. Introduction

Since the introduction of microfluidic paper-based analytical devices (μPADs) in 2007, the field of paper-based diagnostics has expanded rapidly (Martinez et al., 2007). The use of paper for diagnostic purposes was reported as far back as the early 1900s (Dieterich, 1902; Yetisen et al., 2013). However, it was not until the 1950s when modern paper-based diagnostics were first reported with the introduction of the lateral flow assay which was mainly used for home pregnancy tests (Yetisen et al., 2013). Martinez et. al showed how fluidic circuits can be created in paper using simple lithography (Martinez et al., 2007). In the ensuing 14 years, μPADs have been developed for numerous purposes, such as disease diagnosis in human and food samples (Li and Steckl, 2018). Paper provides a number of advantages over traditional microfluidic substrates, such as lower material costs and the ability to wick fluids spontaneously through capillary action, making paper devices more affordable and user-friendly.

Early μPADs were simple, typically using a single fluid type for colorimetric detection (Dungchai et al., 2010; Hossain and Brennan, 2011; Ratnarathorn et al., 2012). However, recent devices have been designed for more complex procedures that require multiple reagents (Park and Park, 2017; Verma et al., 2018). The simplest approach is to manually deposit the reagents at different times. However, this would make the device significantly less user-friendly. Typically, automated

* Corresponding author. Department of Mechanical Engineering, University of California, Riverside, CA, 92521, USA.
E-mail address: htsutsui@engr.ucr.edu (H. Tsutsui).
[1] These two authors contributed equally to this work.

https://doi.org/10.1016/j.bios.2021.113090
Received 7 November 2020; Accepted 10 February 2021

fluid control on μPADs has been achieved by engineering delays on the paper to slow the fluid down. A distance-based delay is the easiest to implement, which consists of increasing the length of the channel (Fu et al., 2010, 2011; Apilux et al., 2013). However, this approach is limited by the footprint of the device as well as the volume of sample because longer channels require more fluid volume to fill them. Additional approaches involve adding dissolvable barriers to temporarily block the flow, placing additional material over the channel to absorb and divert it, or constricting the channel geometry to slow it down (Toley et al., 2013; Shin et al., 2014). These delay methods work but create other issues, such as increased evaporation, which reduces the amount of fluid available for assays.

Untreated paper wicks very slowly because its fibrous network presents narrow and tortuous paths which the fluid must follow along (Elizalde et al., 2015; Castro et al., 2017). Efforts to accelerate wicking in paper channels have included either sandwiching the paper between polymer films (Jahanshahi-Anbuhi et al., 2014; da Silva et al., 2015), creating a two-ply structure (Camplisson et al., 2015; Channon et al., 2018), physically modifying pore sizes by laser ablation (Kalish et al., 2020), or by removing regions of the paper to create 'macro capillaries' for the liquid to flow through (Renault et al., 2013; Giokas et al., 2014; Shin et al., 2016; Liu et al., 2017). Of interest is the work of Giokas et al. and Liu et al., who demonstrated that creating parallel grooves onto paper channels using either a plotter or a CO_2 laser can lead to much faster wicking speeds.

A recent development in the field is the paper-based chemiresistive biosensor. Utilizing single-walled carbon nanotubes (SWNTs), this type of sensor can detect analyte concentrations based on changes in the electrical properties of the SWNTs. Current label-based electrochemical sensors lack appropriate markers for all types of analytes. Additionally,

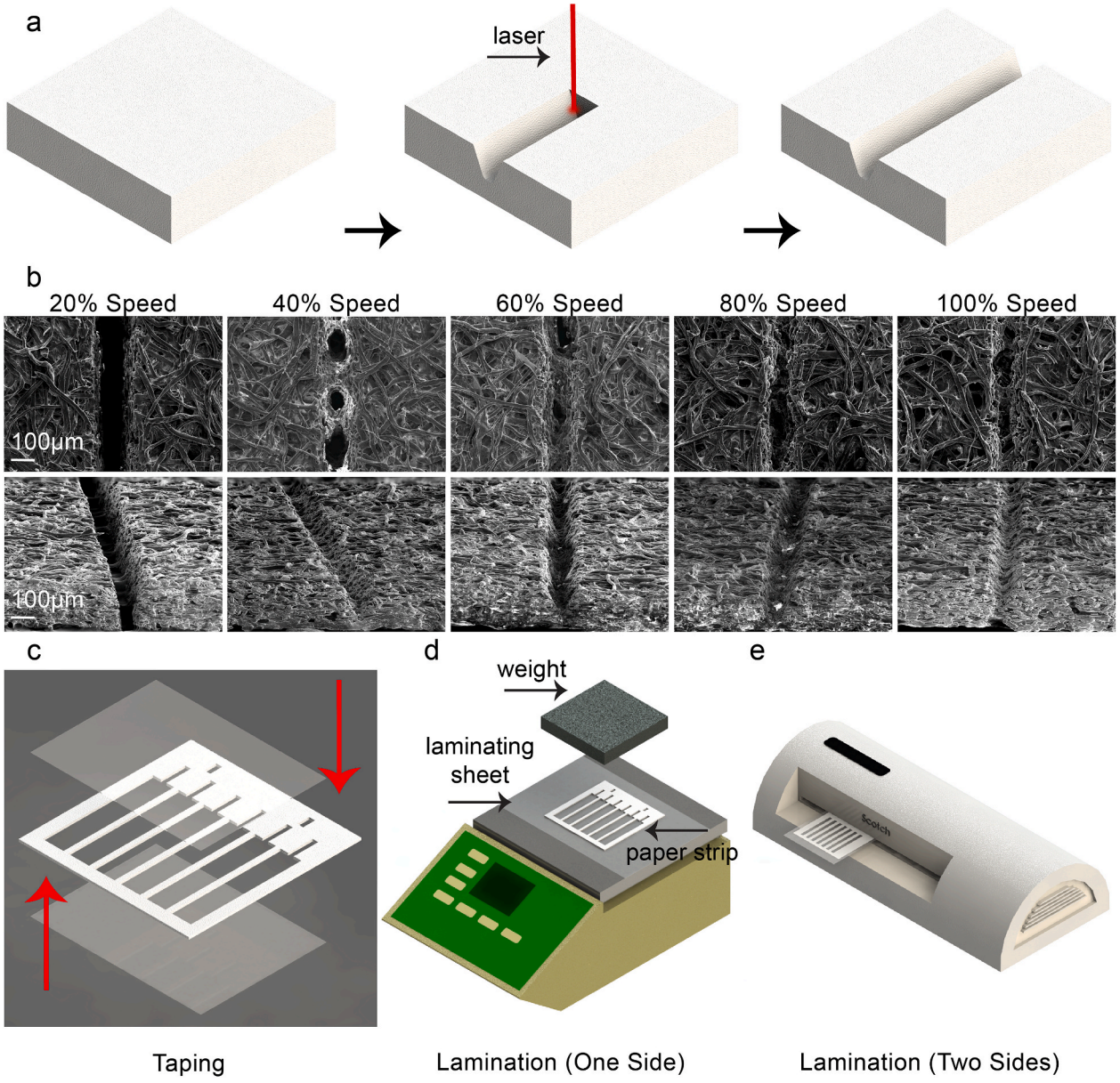

Fig. 1. Fabrication of paper-based microfluidic test devices featuring laser-etched grooves (a) Schematic summarizing fabrication of laser-etched grooves on paper. As the laser beam passed the paper, it burnt away some of the material, leaving behind a groove. (b) SEM images of grooves etched at different speeds. Note that while the width of the groove was consistent, the depth was inversely proportional to the etching speed. (c) Taped channels were made by applying tape to one side of the paper strip or both. (d) Laminating only one side of a paper strip was done by heating the laminate on a hot plate at 150 °C and pressing the paper onto it with a weight. (e) Laminating on both sides was done by simply putting the paper strip inside a laminating pouch and passing it through a conventional laminator (5mil thickness setting).

these sensors require larger fluid volumes to accommodate the necessary redox reactions. By contrast, chemiresistive biosensors are label-free and provide accurate, quantitative data with lower limits of detection (LOD) compared to traditional electrochemical sensors (Villamizar et al., 2008; Yamada et al., 2014; Shen et al., 2019, 2021). In this study, we build upon the work of Giokas et al. and Liu et al. (Giokas et al., 2014; Liu et al., 2017) by conducting a more thorough analysis of laser-etched grooves on paper. In addition to finding optimum groove parameters, we demonstrated the use of laser-etched grooves on paper for sequential delivery for a chemiresistive biosensor, which we recently reported (Shen et al., 2019).

2. Materials & methods

2.1. Groove fabrication

Groove designs were created in Adobe Illustrator CC (Adobe Inc, San Jose, CA). As shown in Fig. 1a, Whatman 4 filter paper (GE Healthcare, Chicago, IL) was cut out and etched using an Epilog Zing 16 30W CO_2 laser cutter (Epilog Lasers, Golden, CO). Laser power and frequency were set at 5% and 5000 Hz respectively, while laser speed was varied between 20% and 100% to etch grooves with different depths. The nominal thickness of untreated filter paper is 180 μm.

2.2. Groove characterization - mass loss

Mass loss was assessed by weighing 50 mm × 50 mm squares etched with grooves at different speed settings. Grooves were etched with a center-to-center spacing of 350 μm (~137 linear grooves/square). Samples were weighed using a model TP-64 analytical balance (Denver Instrument, Bohemia, NY).

2.3. Groove characterization - cross-sectional area assessment

Visualization of the grooves and their cross-sections was achieved using a Nova NanoSEM 450 scanning electron microscope (SEM) (FEI, Hillsboro, OR). Prior to imaging, paper samples were coated with platinum/palladium using a Cressington 108 Auto Sputter Coater (Cressington Scientific Instruments, UK). Groove morphology at different speed settings was characterized by measuring the cross-sectional area for each groove relative to the total thickness of the paper. Measurements were made using ImageJ (NIH, Bethesda, MD). A 'unit cell' was drawn around each groove, with a width equal to the top width of the groove and a height equal to the thickness of the paper. The fraction of the unit cell that was taken up by the groove was assessed using the polygon tool in ImageJ.

2.4. Vertical wicking

Vertical-wicking test strips were designed in Adobe Illustrator CC. Each test strip has six channels (2 mm × 40 mm), consisting of one blank (unetched) channel and five channels each with a single groove (etched at a different laser speed) in the center of the channel. Grooves were defined in Illustrator as line segments. Wicking experiments were performed in a humidity-controlled chamber (Model 5503-E, Electro-Tech Systems, Glenside, PA) kept at 99% relative humidity (RH). This high RH minimizes effects of evaporation. Each test strip was mounted vertically to a testing rig and placed inside the chamber (Fig. S1). All channels were tested without washing or other chemical treatments.

A small reservoir of deionized (DI) H_2O was placed onto a laboratory jack (Model L-490, Thorlabs, Newton, NJ) situated beneath the test strip. The jack was raised until the water touched the bottom of the strip, allowing wicking to commence. Wicking fronts were recorded using a Nikon D5100 camera (Tokyo, Japan) fitted with a Tamron macro lens (Saitama, Japan). Video files were processed into individual frames using Adobe Premier Pro CS6 (San Jose, CA). Wicking distances were then recorded using ImageJ's Manual Tracking plug-in.

2.5. Sealed channels

The previously described wicking experiments were repeated with channels sealed with different tapes. The ones used in this study were 3M Scotch Heavy Duty Shipping Packaging Tape (3M, Two Harbors, MN), MD Weatherstrip Tape (MD Building Products, Oklahoma City, OK) and Uline S-423 Industrial Tape (Uline, Pleasant Prairie, WI). Channels were sealed on the front (side with the groove) or back only and on both sides (Fig. 1c). Additionally, paper channels were sealed using thermal laminating pouches (3M, Two Harbors, MN) (Fig. 1d and e). To laminate the channels on front/back only, a single laminating sheet was placed onto a hot plate (Torrey Pines, San Diego, CA) set to 150 °C. The paper channel was placed on top of the laminating sheet and held there with a small weight for three minutes to insure a proper seal. Channels laminated on both sides were passed through a Scotch Thermal Laminator (3M, Two Harbors, MN) using the 5mil thickness setting.

2.6. Wider grooves

Wicking test strips with wider grooves were created in a similar manner to regular wicking test strips. Rather than defining a groove using a line segment, rectangles with various widths (50 μm–200 μm) were instead used to define wider grooves. Laser settings were fixed at 20% speed and 5% power. Channels were tested untaped and sealed on both sides with Uline S-423 Industrial Tape.

2.7. Groove pitch optimization

Groove designs were made in Adobe Illustrator, as in the previously described tests. Vertical test strips had channels which were 6 mm wide and 40 mm long. Grooves were etched using the CO_2 laser (speed setting: 20%, power setting: 5%) at different center-to-center pitches, ranging from 0.1 mm to 3 mm. Vertical wicking experiments that were identical to those described above were conducted on untaped channels and channels sealed on both sides with Uline S-423 Industrial Tape.

2.8. Effect of increased viscosity

Additional wicking experiments were conducted with 10%, 20% and 35% (v/v) glycerol (Fisher Scientific, Pittsburgh, PA) in DI H_2O. These solutions have viscosity values corresponding to 1.38 cP, 1.98 cP and 3.76 cP at 20 °C, respectively (Cheng, 2008; Volk and Kähler, 2018). Channels were tested untaped and taped on both sides with Uline S-423 Industrial Tape. Each test strip had 3 unetched, blank channels and 3 channels etched at 20% speed. Wicking experiments were conducted as described in section 2.4.

2.9. Demonstration device for sequential delivery and analyte detection

The demonstration device utilizes a paper-based chemiresistive biosensor employing SWNTs, which we recently reported (Shen et al., 2019). To fabricate this sensor strip, SWNTs (P3-SWNTs, Carbon Solutions, Inc., Riverside, CA) and pyrene carboxylic acid (PCA) (Tokyo Chemical Industry Co., Ltd. Portland, OR) were dispersed in dimethylformamide (DMF) (Fisher Scientific, Pittsburgh, PA) through sonication. The mixture was then filtered to collect the PCA/SWNT aggregates, which were washed several times with methanol/DI H_2O and dispersed in DI H_2O. The sensor base was made by printing wax ink (Xerox ColorQube 8880, Xerox, Norwalk, CT) onto a strip of Whatman 5 filter paper (GE Healthcare, Chicago, IL). The wax was melted at 170 °C for 5 min to create hydrophobic boundaries throughout the thickness of the paper. A second layer of wax was printed but not melted to ensure sufficient hydrophobicity at the paper surface. The paper channels were placed on a glass frit with a vacuum (~80 kPa) underneath, and the

PCA/SWNT dispersion was dropped onto the sensing channel to deposit the PCA/SWNTs. Source and drain electrodes were created by applying silver paste (Ted Pella Inc. Redding, CA) onto either end of the sensor. Anti-human serum albumin (anti-HSA) antibody (BiosPacific, Inc. Emeryville, CA) was immobilized on the SWNT channel using EDC/NHS chemistry. This was followed by quenching remaining active groups with 0.1 M ethanolamine (Fisher Scientific, Pittsburgh, PA) and blocking non-specific binding with 0.1 wt% Tween-20 (Bio-Rad, Hercules, CA). The dry initial resistance of the sensing channels after functionalization, quenching, and blocking was 9.90 ± 0.31 kΩ.

The rest of the demonstration device consisted of a fluid-handling layer, which facilitated rapid, sequential delivery of a sample and wash buffer and waste pads that absorbed excess fluid as it passed through the sensor. Both fluid-handling and waste layers were constructed from Whatman 4 filter paper and cut out using the CO_2 laser. The device itself was constructed using a bottom-up approach. A strip of Uline tape was placed adhesive-side up onto a piece of thick, double-sided tape (Style-592, Intertape Polymer Group, Newport Beach, CA). This double-sided tape acted as a rigid support for the device. The waste pad was then attached to the Uline tape, followed by the sensor and the fluid-handling layer on top of that. Another piece of Uline tape was placed on top of the fluid handling layer to seal together this three-layer sandwich. This top layer of tape had holes cut into it to allow addition of sample and wash buffer and to connect electrodes to the sensor for electrical measurement.

All electrical measurements were carried out using a potentiostat (model 600E, CH Instruments, Austin TX) as previously reported (Shen et al., 2019). Flat alligator clips were connected to the silver conductive pads. Electrical measurements were performed by measuring the I–V curve using linear sweep voltammetry (LSV) from −0.1 V to 0.1 V. The reciprocal of the slope of the curve was the resistance of the sensor. Real-time monitoring was done by amperometric monitoring of current vs. time with a source-drain bias at 0.1 V.

Devices were tested by first priming the chemiresistive sensor with 20 μL of 10 mM phosphate buffer (PB) (pH 7.4), which was added to the sample inlet and allowed to saturate the sensor for 2 min. HSA solutions were prepared using PB, artificial urine (AU) and artificial saliva (AS). AU and AS formulations were adapted from previous studies (Brooks and Keevil, 1997; Tlili et al., 2010). Preparation of AU included the following: 170 mM urea, 90 mM KCl, 90 mM NaCl, 25 mM NH_4Cl, 7 mM creatinine, 7 mM K_2HPO_4, 7 mM KH_2PO_4, 2.5 mM $CaCl_2$, 2 mM $MgSO_4$, 2 mM $MnCl_2$, and 0.4 mM uric acid mixed together in DI H_2O with pH adjusted to 7.4. AS consisted of 0.6 g/L of Na_2HPO_4, 0.6 g/L of anhydrous $CaCl_2$, 0.4 g/L of KCl, 0.4 g/L of NaCl, 4 g/L of mucin and 4 g/L of urea dissolved in DI H_2O with pH adjusted to 7.4. Then, 20 μL of HSA (Sigma-Aldrich, St. Louis, MO) sample (prepared at varying concentrations in PB, AU, or AS) and another 60 μL of 10 mM PB were simultaneously added to the sample and wash buffer inlets, respectively. Measurements were taken until the output current achieved steady state.

3. Results and discussion

3.1. Groove fabrication

Fig. 1b shows SEM images of grooves that were etched at different speeds. As speed decreased, the laser burned away more material and made a deeper groove. The slowest speed tested (20%) allowed the laser to cut through the paper, creating a slit. A speed setting of 40% created characteristic holes in the paper, spaced evenly throughout the length of the groove. The laser module is driven by stepper motors, which cause the module to move in a series of 'steps' rather than continuously. Therefore, the laser spends slightly more time at a region that corresponds with the end of a step, burning more material there. This phenomenon was seen to a lesser extent in grooves etched at faster speeds. A secondary contribution could also come from the non-homogenous fiber density in the paper. Certain regions may have more densely packed fibers than others due to variability in the manufacturing process (Alava and Niskanen, 2006).

The second row of Fig. 1b shows perspective SEM images of grooves that were etched at different speeds. Grooves etched at 20% have a trapezoidal cross-section. Since the focus of the laser was on the paper surface, power density was reduced at any point below, causing the laser to burn through less material. Grooves etched at the other speeds exhibited roughly v-shaped cross-sections of varying depths. All grooves were ~175 μm wide at opening.

3.2. Groove characterization

The morphology of the laser-etched grooves was characterized by analyzing the depth of each groove relative to the thickness of the paper as well as mass loss caused by each groove. Measurements indicated that slits (20% speed) reduced the cross-sectional area of the paper by ~60% (Fig. S2a). Grooves etched at faster speeds reduced the cross-sectional area by lesser amounts. A linear relationship was observed between etching speed and cross-sectional area (Fig. S2c). Mass loss experiments determined that slits reduced the mass of the paper by roughly 15% (Fig. S3b). Again, a linear relation was observed between mass loss and etching speeds. More detailed information regarding these relationships can be found in Supplemental Figs. S2 and S3.

3.3. Vertical wicking – No tape & Uline taped channels

Fig. 2 shows distance vs. time plots for untaped channels as well as channels sealed on various sides using Uline S-423 Industrial Tape. This tape was chosen here because our lab has used it in the past to fabricate multilayer paper devices. With a thickness of only 50.8 μm, the tape was very easy to fold around edges/creases to seal different layers of paper together. Untaped grooves etched at all speeds created faster wicking channels compared to untreated paper with the fastest wicking occurring in channels etched at 20% speed (Fig. 2 No Tape). The grooves acted as macro capillaries with a lower flow resistance compared to the paper around it. This allowed fluid to travel outside the paper matrix and serve as a secondary fluid source above the waterline for the paper, resulting in faster overall wicking. Since a 20%-speed groove was etched completely through the paper, it had the largest macro capillary, making it the fastest, which indicated that cutting a slit into the channel was the optimal way to speed up fluid delivery.

In general, the same trend was seen for taped channels. However, etched channels with tape were generally faster than their untaped counterparts. Moreover, wicking speeds seemed to depend on which side of the channel was sealed. When channels were sealed only on the front, grooves etched at all speeds wicked more quickly (Fig. 2 Uline S-423 Front Only). The tape provided extra surface area which increased contact forces between the liquid and the capillary. Without tape, the surrounding paper tends to flex/swell during wicking, which can destabilize the capillary and slow fluid down. Since the tape was applied to the side that was etched, fluid inside the macro capillary in all groove types benefited from the extra surface area, which made all the etched channels faster. Regarding the 20%-speed grooves, taping the slit even on one side stabilizes the macro capillary in the center. On the other hand, sealing channels only on the back improved wicking in channels etched at all speeds but to a lesser extent (Fig. 2 Uline S-423 Back Only). Since grooves etched at faster speeds did not extend all the way through the paper for the entire groove length, there was less interaction between the fluid within the capillary and any tape on the back side. Thus, much smaller differences in wicking speeds were observed relative to the untaped channels. Applying tape to both sides had a similar effect to applying tape on the front side for channels etched at lower speeds (Fig. 2 Uline S-423 Both Sides). However, channels etched at faster speeds along with blank channels wicked somewhat slower. One possible reason was that sealing the paper on both sides blocks pores that lead to the surface of the paper. Without tape, fluid could run along

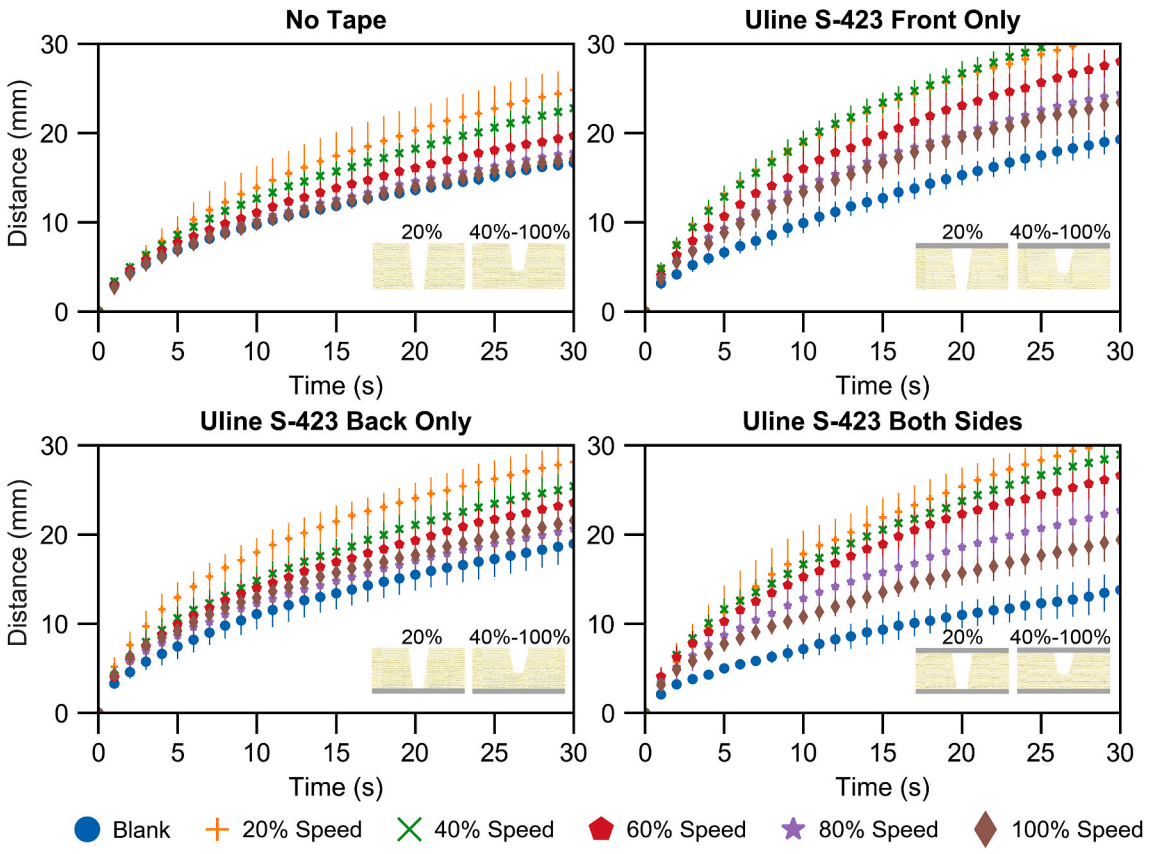

Fig. 2. Distance vs. time plots for grooves with different etching speeds without tape and taped in various configurations with Uline S-423 Industrial Tape. Insets show tape configurations relative to groove geometries. With or without tape, grooves etched at 20% wicked the fastest. Wicking performance was strongly dependent on which side of the channel was taped. Data presented as mean ± SD. N = 10.

the outer surfaces of the paper, which had a lower flow resistance than the porous matrix of the paper. With the tape in place, all the fluid must flow within the paper, forcing it to move more slowly.

3.4. Vertical wicking – sealed channel comparison

Further investigation was performed to learn how sealing grooved channels with different types of tape/sealing would affect their wicking behavior. Preliminary tests were conducted using 3M Scotch Heavy Duty Shipping Packaging Tape (Fig. S4). However, this tape was very susceptible to lifting off when the paper beneath it was wet, causing a great deal of variability. We repeated experiments with tapes that were more fluid resistant. In addition to the Uline tape, the MD Weatherstrip tape was selected as it was typically used to seal window frames to protect against moisture. Additionally, lamination has been commonly used to protect documents against liquid and has been used to make paper-based devices in the past (Ota et al., 2018). Both the Uline and MD tapes were slightly hydrophobic (contact angles 109° and 106°, respectively) while the lamination sheet was weakly hydrophilic (83°) (Fig. S5). Fig. 3 shows distance vs. time plots for all three sealing methods for blank channels and grooved channels etched at 20% speed and 60% speed. The Uline and MD tapes followed a similar trend. However, laminated channels were much slower, despite the lamination sheet having a more hydrophilic surface. Lamination was accomplished by heating up the laminating sheet and applying force to press it onto the paper. It appeared that the adhesive on the lamination sheet melted and seeped into the paper, blocking some pores. This slowdown was dramatic enough that a 20%-speed groove laminated on both sides was no faster than its untaped counterpart (Fig. 3).

The theoretical capillary rise for through-cut grooves of different widths (taped and untaped) is plotted in Fig. S6a. This was done by assuming that the grooves had a capillary with a rectangular cross section and the walls were impermeable. This simple capillary model suggests that laminated channels should have the highest capillary rise, due to the relative hydrophilicity of the laminate sheets and the extra surface area fluid can interact with. This implies that these channels should wick the fastest. However, as described above, laminated channels were slowest among the sealed channels and even slower than untaped channels in certain configurations. Moreover, the Uline and MD tapes should theoretically be the slowest, as the hydrophobicity of the adhesive would impede the rise of fluid within the capillary. Wicking data showed the opposite trend. Channels sealed with these tapes were generally faster than laminated channels. Additionally, the model suggests that a smaller capillary will have a higher capillary rise and should wick more quickly. However, we found that etching completely through the paper (20%-speed grooves), which created the largest macro capillary, was in fact the fastest. This discrepancy between the model and experimental results is mainly because the simple capillary model did not consider transport of fluid between the groove and surrounding paper pores. These pores continuously draw fluid out of the groove as it moves up along the channel. Since shallower grooves have more paper surrounding them, they are presumably losing more liquid and thus rise more slowly.

3.5. Vertical wicking – channels with wider grooves

Having observed that cutting a slit in the paper created the fastest wicking channels (Fig. 2), our next goal was to determine the optimal geometry that would create the fastest channels. We decided to expand the width of the groove, reasoning that a wider capillary would allow more fluid to flow in between the paper and thus make the channel faster. As described earlier, rectangles with different widths were used to

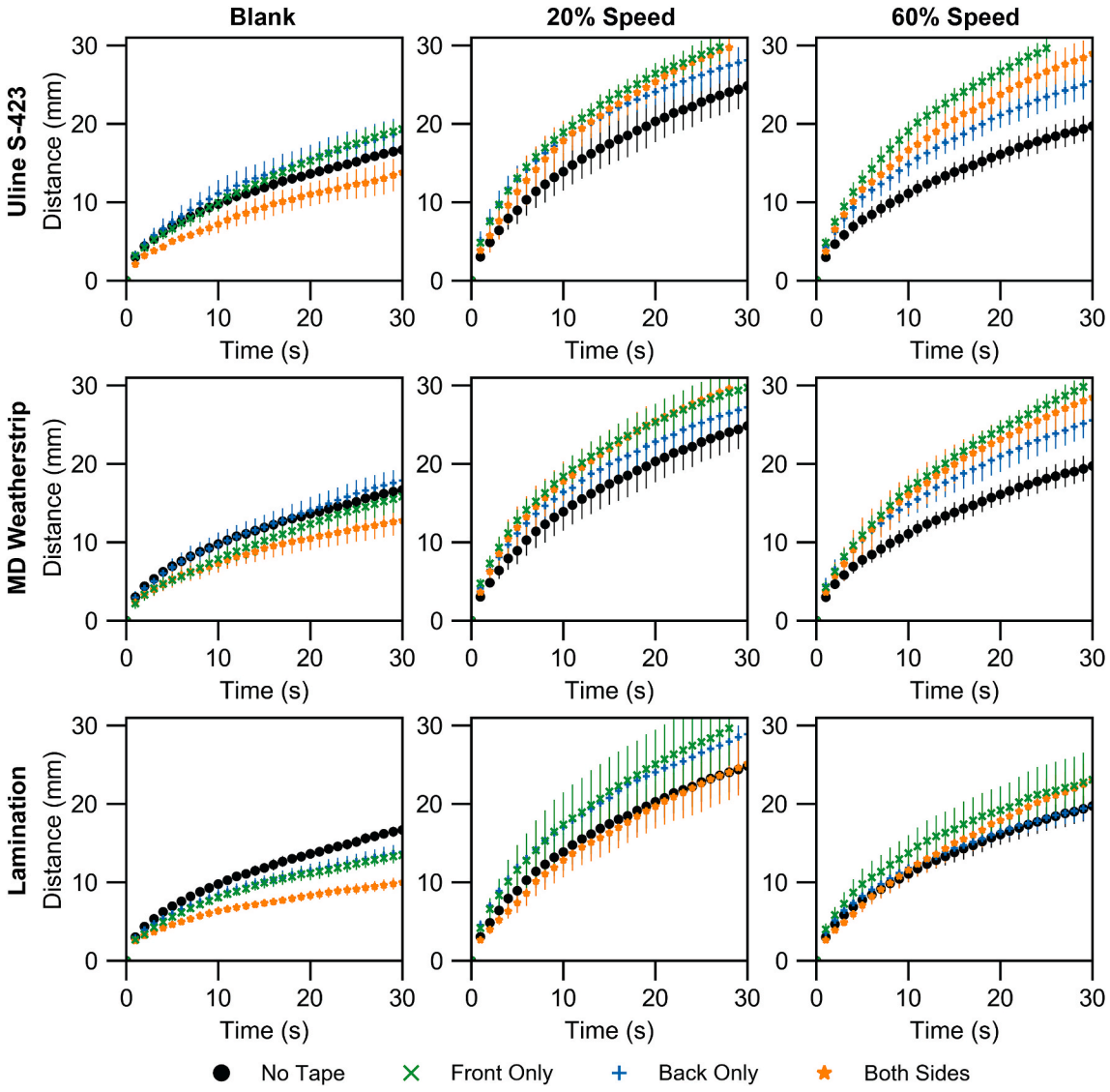

Fig. 3. Distance vs. time plots for grooves with different etching speeds without tape and taped in various configurations with various tapes. Wicking performance was strongly dependent on what type of tape was used to seal the channels. Data presented as mean ± SD. N = 10.

create wider grooves. Fig. 4a shows SEM images of wider grooves and the width of the rectangles used to create them. The smooth edges presented on the +150 μm and +200 μm grooves were due to ash that has accumulated from the laser-etching process. The same 6-channel test strip design used previously (Fig. S1b) was used in these experiments, with the four wider grooves compared to the original groove etched at 20% speed and a blank, unetched channel.

Distance vs. time plots in Fig. 4b show that the original 20%-speed groove wicked faster than any of wider grooves without tape. The theoretical capillary rise for through-cut grooves of different widths is plotted Fig. S6a. As the width of the groove increases, the theoretical height of the fluid in the capillary decreases. The weight of the fluid increases more quickly if the capillary is wider, canceling the surface tension force more quickly. Therefore, the liquid would rise to a lower height in wider capillaries, which explained why those channels wicked more slowly. For untaped channels, it appeared that very little fluid entered the capillary in the wider-groove channels, given their similarity to the blank channel. Without this meniscus in the center, the fluid moved up in a pair of narrower and separated paper strips. The reduced cross-section of each strip resulted in slower wicking overall.

With regards to groove width, theory suggests that wider grooves should have a lower capillary rise (thus slower wicking speed in the channel) regardless of how the channels are sealed (Fig. S6a). While untaped channels behaved according to this trend, taped channels performed less predictably (Fig. 4b). The 20% speed, +50 μm and +100 μm channels wicked at roughly the same speed. Nonetheless, the original 20%-speed groove consistently wicked the fastest in both taped and untapped configurations, and hence used in the subsequent investigations.

3.6. Groove pitch optimization

Having established the optimal laser and geometry settings for a single groove, it was important to determine the ideal number of grooves to place in a single channel. Whatman 4 filter paper test strips with 6 mm × 40 mm channels were etched with grooves of varying pitches. Fig. 5a shows all the pitches that were explored. Rather than measuring the wicking front over time, we simply measured the time needed for the wicking front to reach the top of the channel (Fig. 5b).

As shown in Fig. 5b, untaped channels had an optimal pitch of 0.75 mm. At smaller pitches, the excessive removal of material made the paper channel more unstable. There was excessive bending/buckling of the paper which disrupted wicking. The 0.2 mm and 0.1 mm pitch channels were destroyed and did not wick completely because the

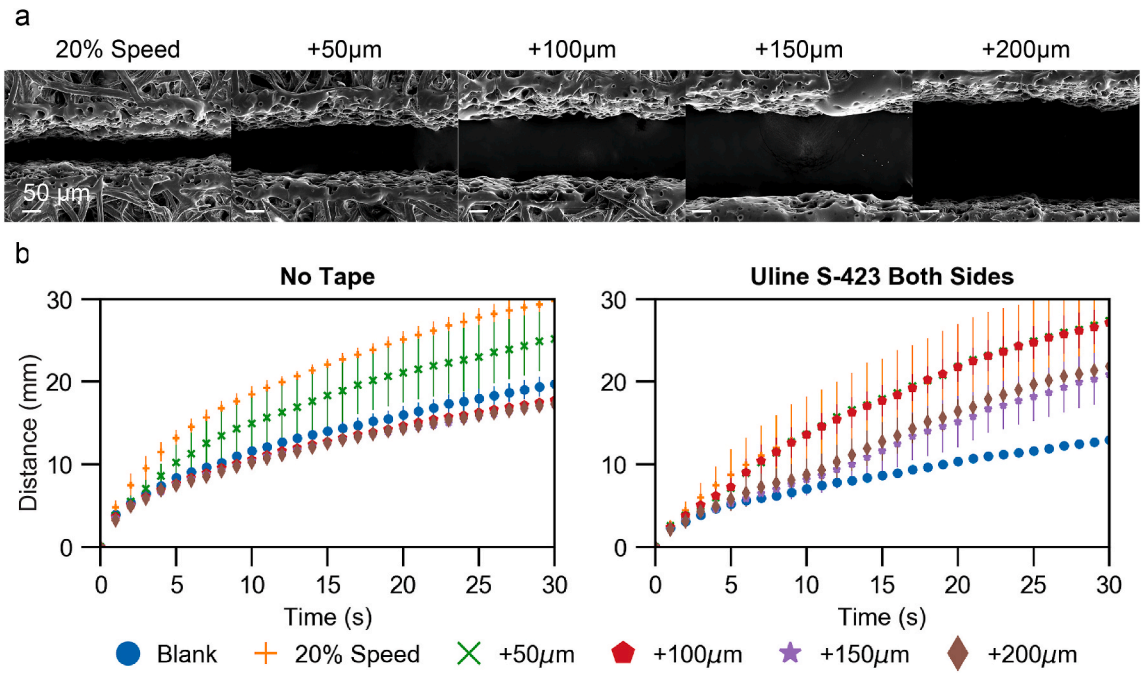

Fig. 4. Characterization of wide groove channels. (a) SEM images of 'wide' grooves that were etched by cutting rectangles in the paper channel with the CO_2 laser. The '20% Speed' groove was the original groove cut using a straight line, while the wider grooves were designed using rectangles of specified widths. Scale bar = 50 μm. (b) Distance vs. time plots for wide grooves in untaped and taped configurations. Data presented as mean ± SD. N = 5.

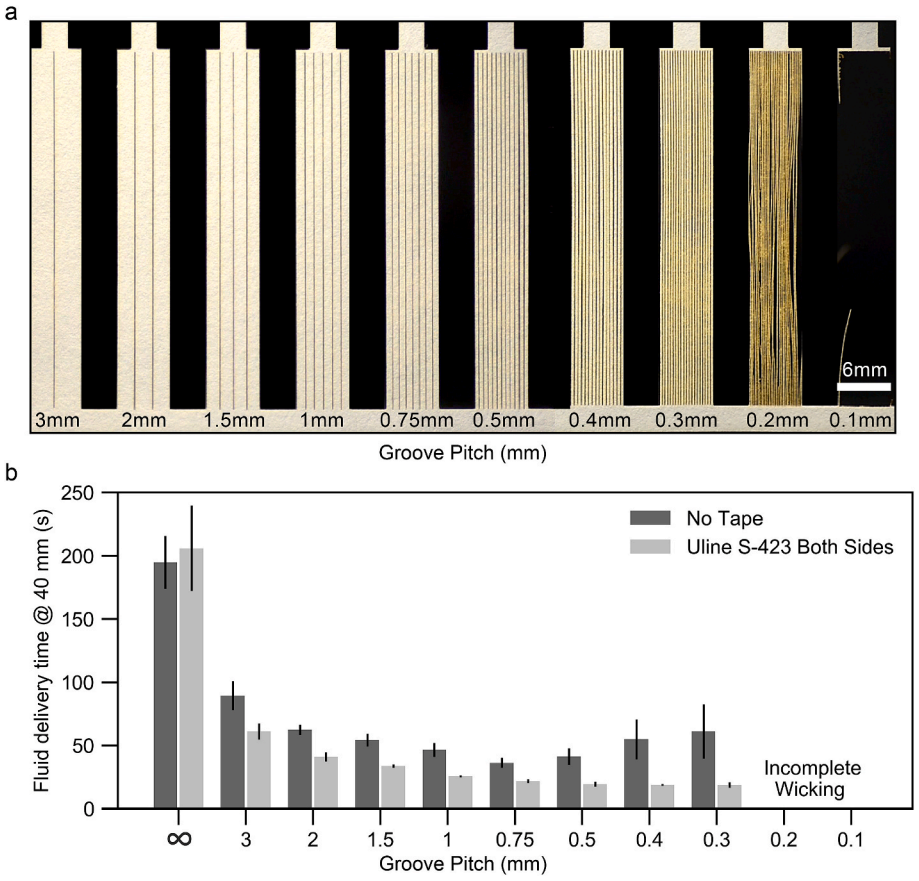

Fig. 5. Groove pitch optimization. (a) Image of test strip used to test groove densities. Channels were 6 mm wide × 40 mm tall. Groove pitch is the center-to-center distance between adjacent grooves. Below 0.3 mm, the grooves are spaced within the resolution of the laser, which means that most of the paper was burned away. Scale bar = 6 mm (b) Fluid delivery times for different groove densities in taped and untaped (Uline S-423) configurations. A groove pitch of 0.75 mm was chosen as optimum. Data presented as mean ± SD. N = 5.

groove pitch was below the resolution of the laser. This means that the laser passed over the same region of paper multiple times and burnt it away. Taped channels did not yield an optimal value. Rather, there were diminishing gains in wicking speed as more grooves were added. As stated before, sealing the channels with tape helps stabilize the macro capillaries that formed inside each channel. A pitch of 0.75 mm was

selected as optimum due to negligible reduction in wicking time for grooves with higher densities. Additionally, having to etch fewer grooves reduced fabrication times. For both taped and untaped channels, it was interesting to note the dramatic reduction in wicking time when only a single groove is added to an unetched channel (~50% and ~70% respectively).

Our discovery that a through-cut groove has the fastest wicking speed matched the results of Liu et al. (2017) who reached the same conclusion using different laser settings. However, while our experiments employed vertical wicking studies, they used horizontal wicking. This means that the effect of gravity was negated in their experiments. This key difference may explain why their reported wicking speeds were much higher than ours (~59-fold improvement in avg. velocity vs ~8-fold). Our results show that gravity can play a significant role in wicking performance, as the rise of the fluid inside the macro capillary is slowed down by the weight of the fluid itself. Additionally, Liu et al. achieved fastest wicking with a groove pitch of 0.375 mm (8 grooves in a 3 mm channel) vs. 0.75 mm from our findings. Both groups found that taping channels can make them wick much faster. However, our findings show that the type of sealing tape employed played a significant role in

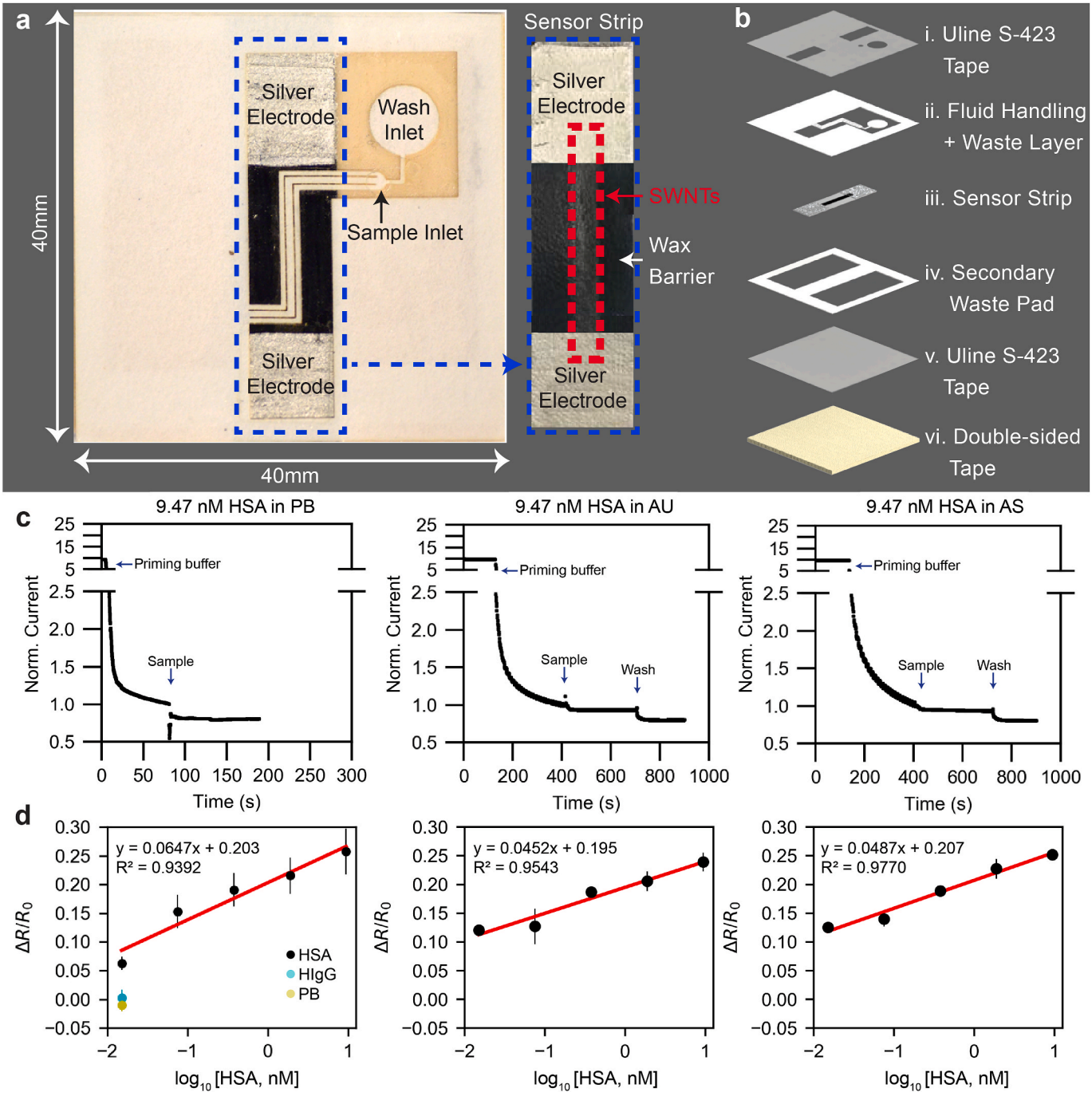

Fig. 6. Overall design and demonstration of the paper-based chemiresistive sensor device. (a) Images of the assembled multi-layer device (left) and the sensor strip inside (right). (b) Schematic of the multi-layer assembly, showing the fluid-handling layer, the chemiresistive sensor strip, and the other layers. (c) Current response for a fixed concentration of HSA (9.47 nM) in PB, AU and AS. Current is normalized with respect to the current after priming. Plots for both artificial biological fluids show the need for a washing step for signal recovery compared to PB. (d) Calibration plot of normalized change in resistance for each fluid type. Data presented as mean ± SD. N = 3.

wicking speeds (i.e., lamination vs. tape). Additionally, we found that certain tapes influence wicking differently based on what side of the channel is sealed (etch-side up or down).

GIF files of all previously discussed wicking experiments can be found in the Supplementary material provided.

3.7. Effect of increased viscosity

At room temperature (20 °C), water (1.002 cP) (Korson et al., 1969) is less viscous compared to body fluids such as plasma (1.81 cP) (Lowe, 2019), saliva (2.45 cP) (Kusy and Schafer, 1995), 20% hematocrit blood (3.8 cP), and 40% hematocrit blood (6.3 cP) (Rand et al., 1964). We repeated the vertical wicking experiments with 10%, 20% and 35% (v/v) concentrations of glycerol in DI H_2O to simulate the behavior of different biological fluids in our device. At an ambient temperature of 20 °C, the dynamic viscosities of the three solutions were 1.38 cP, 1.98 cP and 3.76 cP, respectively (Cheng, 2008; Volk and Kähler, 2018). Additionally, since the dynamic viscosity of urine at 20 °C is 1.09 cP (Elkins et al., 1974; Inman et al., 2013), its viscosity is comparable to that of water. For unetched channels, increasing the viscosity of the fluid reduced wicking speed (Fig. S7). Even 10% glycerol reduced wicking speed by roughly half. However, wicking in grooved channels for each type of fluid was still significantly faster than their unetched counterparts. Wicking of the 35% glycerol solution was roughly twice as fast in the grooved channels compared to the unetched channels. These data show that grooves can dramatically increase wicking speeds even in viscous fluids.

3.8. Demonstration device for sequential delivery and analyte detection

The optimization studies conducted on laser-etched grooves were used to design a fluid-handling mechanism for the chemiresistive paper-based sensor. The main goal of the fluid-handing mechanism was to sequentially deliver a sample and wash buffer to the chemiresistive sensor without any user intervention after initial depositions of fluids. In our previous report (Shen et al., 2019), both the sample and wash buffer were manually applied by pipet and removed by vacuum filtration in sequence, requiring substantial user intervention. In addition, a vacuum source might not be readily available in resource-limited or in-field settings.

As shown in Fig. 6a, the location of the sample inlet provided the liquid with two possible directions to flow, either towards the etched channel to the sensor or towards a narrow channel to the wash buffer inlet. Because the grooved channel had a much lower resistance to flow, almost all the sample flowed in that direction. The grooved channel rapidly delivered the sample across the surface of the chemiresistive sensor that was positioned directly underneath. Additionally, since the grooves were slits, they allowed bulk fluid to directly contact the sensor, improving mass-transfer kinetics and reducing time required for reaching stable signals. A secondary waste pad (Fig. 6b iv) sat directly below the sensor and absorbed any fluid that passed through it, reducing accumulation of 'depleted' sample fluid at the sensor surface. Excess sample also flowed into the waste-pad region at the end of the grooved channel. Since the channel was presaturated with fluid, the wash buffer did not start moving downstream until the sample solution in the sample inlet was sufficiently depleted. Fig. S8 shows a time-lapse of the aforementioned sequential delivery step.

Since the SWNT chemiresistor sensor is highly sensitive to its environment, priming buffer was needed to fully moisturize the sensor before sample was introduced. The assembled devices showed a stable current around 10 μA with a source-drain voltage of 0.1V, because of its initial dry resistance of 9.9 kΩ. However, the current decreased significantly upon the addition of the priming buffer (20 μL 10 mM PB, pH 7.4) due to a large addition of water molecules onto the chemiresistor (Fig. 6c). Water molecules in the priming buffer n-doped the p-typed SWNTs and thus caused the observed decrease in the current through a dramatic increase in the resistance (Han et al., 2012; Shen et al., 2019, 2021). As shown in Fig. 6c, sample added after the priming process flattened the baseline current. Normalization based on the primed baseline was an essential step for reading the electrical responses. Normalized current was defined as the ratio of the raw current (I) and the current after the priming process (I_p). As shown in Fig. 6c, the normalized current was, by definition, at 1.0 at the point of sample arrival and decreased as more HSA sample was delivered to the sensor. In PB at pH 7.4, HSA molecules carried a net negative charge and were specifically bound to the anti-HSA. The binding events transferred charge to the semiconducting SWNTs. The SWNT chemiresistive sensor responded to the charge change at the sensor's surface due to the dominating effect of electrostatic gating (Shen et al., 2019). Fig S9 contains current vs. time plots for different concentrations of HSA in PB and controls.

A linear calibration curve with a satisfactory sensitivity and specificity was obtained over a wide range between 0.015 nM and 9.47 nM. As shown in Fig. 6d, the calibration curves were graphed as $\triangle R/R_0$ vs. Log_{10}[HSA, nM], where ΔR was the difference between the steady-state resistance R after sample incubation and wash and the resistance R_0 after the sensor was primed (before sample addition). The response was linear with a 6.47% increase in the resistance per Log_{10}[HSA, nM]. Controls were tested by adding the same volume of PB or a non-target protein (9.47 nM human immunoglobin G (HIgG) in 10 mM PB, pH 7.4). PB alone introduced a $-1.01 \pm 1.1\%$ change after normalization, while the non-target crosstalk control (HIgG) resulted in only a $0.289 \pm 1.4\%$ change. By comparing the responses from the PB blank ($\triangle R/R_0 \pm 3SD$) and the responses from 15 pM HSA in PB ($\triangle R/R_0 \pm SD$), the lowest detectable concentration of HSA in PB was 15 pM based on an S/N ratio of 3 ($p = 0.023 < 0.05$). This figure is superior to traditional HSA biosensor LODs in the milligram per milliliter or micromolar range (Choi et al., 2004; Aliño and Yang, 2011). These results indicated the high sensitivity and specificity of the biosensor.

Furthermore, to mimic the detection of HSA in real samples, we challenged the device with HSA samples in complex matrices, such as AU and AS. Due to the elevated level of dissolved salts in the AU and AS, the local ionic strength near the sensor surface was high and led to a minimal Debye length. Thus, it was necessary to use PB washes to dilute the local ionic solution and recover the electrical responses corresponding to the affinity-based binding between the antigen and antibody (Kaisti, 2017; Shen et al., 2021). As shown in Fig. 6c, after PB priming, the HSA sample in AU or AS matrix gave a reduced response (less decrease in the current) compared to that in HSA samples in PB. A 60 μL PB wash was used to recover the responses (more decrease in the current). The possible mechanism was that the continuous inflow of PB with low ionic strength washed the salts to the waste layer/pad and diluted the local matrix, which resulted in a larger Debye length to overturn the charge screening and thus recovered the responses (Kaisti, 2017; Shen et al., 2021). These observations show that a well-controlled fluid delay is an essential function for a paper-based microfluidic biosensor for more complex, real-life samples. Figs. S10 and S11 contain current vs. time plots for different concentrations of HSA in AU and AS, respectively. The viscosity of the biological samples can also affect their wicking behavior in paper (Fig. S7).

Compared with our previous work (Shen et al., 2019), in which the samples and wash buffers were manually added by pipet and removed by vacuum filtration, the device presented here was ~70% as sensitive with a satisfactory lowest detectable limit of 15 pM HSA in PB. The lower sensitivity for HSA in PB in the current device compared to our prior work is likely because the latter utilized the vacuum filtration to very effectively remove excess sample and wash solution from the sensor surface after incubations. The current device also gave good sensitivities to HSA in AU and AS. The responses were linear with a 4.52% and 4.87% increase in the resistance per Log_{10}[HSA, nM] for AU and AS, respectively. However, devices tested in AU/AS had a ~25%–30% lower sensitivity compared to devices tested with PB only. The lower

sensitivities for HSA in AU and AS were likely because the washing process is even more critical for samples containing ions and other interfering substances. It is expected that the sensitivities can be improved with the revision of the device design to allow for a larger wash buffer volume, which is currently limited to 60 μL. Nevertheless, the sensor still maintained good sensitivity and specificity to HSA. Furthermore, with the new fluid-handling architecture, external devices such as a vacuum filter and a vacuum pump are no longer necessary. The fluid-handling layer was able to semi-automatically deliver the fluids sequentially to the SWNT chemiresistor, thus eliminating the need for specialized personnel.

4. Conclusion

The above work detailed the use of laser-etched grooves to accelerate wicking speeds on paper. Optimization studies were conducted to determine ideal fabrication parameters. It was discovered that the fastest wicking channels were created by simply cutting a slit through the paper. The slit acted as a macro capillary, letting fluid flow outside the paper matrix. The exact mechanisms behind the observed behaviors are not yet well understood and require further investigation. Additional studies found that making the slit wider did not improve wicking performance but sealing the channels did improve wicking speeds. However, the type of adhesive used drastically influences wicking speeds; certain adhesives can slow down the channels, counteracting the enhancement provided by the sealing. An ideal groove pitch was found that balanced the gain in the wicking speed and the structural integrity of the paper channel. As a proof of concept, we successfully demonstrated the utility of laser-etched grooves by enabling rapid, semi-automated sequential fluid delivery for a chemiresistive SWNT paper-based sensor targeting HSA in PB, AU, and AS. Furthermore, it is expected that by combining etching with other fluid control strategies, such as delay shunts or multilayer channels, a much higher degree of wicking control can be available for more complicated point-of-care devices.

Declaration of competing interest

The authors declare that they have no known competing financial interests or personal relationships that could have appeared to influence the work reported in this paper.

Acknowledgements

AM acknowledges the financial support of W. Ruel Johnson Chair. This work was supported by the National Science Foundation under Grant No. 1606181. Any opinions, findings, and conclusions expressed in this paper are those of the authors and do not necessarily reflect the views of the National Science Foundation. Electron microscopy was performed on a FEI Nova NanoSEM 450 in the Central Facility for Advanced Microscopy and Microanalysis (CFAMM) at UC Riverside. The authors thank Dr. Brent Kalish for his assistance in proofreading the manuscript.

Appendix A. Supplementary data

Supplementary data to this article can be found online at https://doi.org/10.1016/j.bios.2021.113090.

References

Alava, M., Niskanen, K., 2006. Rep. Prog. Phys. 69, 669.
Aliño, V.J., Yang, K.-L., 2011. Analyst 136, 3307–3313.
Apilux, A., Ukita, Y., Chikae, M., Chailapakul, O., Takamura, Y., 2013. Lab Chip 13, 126–135.
Brooks, T., Keevil, C., 1997. Lett. Appl. Microbiol. 24, 203–206.
Camplisson, C.K., Schilling, K.M., Pedrotti, W.L., Stone, H.A., Martinez, A.W., 2015. Lab Chip 15, 4461–4466.
Castro, C., Rosillo, C., Tsutsui, H., 2017. Microfluid. Nanofluidics 21, 21.
Channon, R.B., Nguyen, M.P., Scorzelli, A.G., Henry, E.M., Volckens, J., Dandy, D.S., Henry, C.S., 2018. Lab Chip 18, 793–802.
Cheng, N.-S., 2008. Ind. Eng. Chem. Res. 47, 3285–3288.
Choi, S., Choi, E.Y., Kim, H.S., Oh, S.W., 2004. Clin. Chem. 50, 1052–1055.
da Silva, E.T., Santhiago, M., de Souza, F.R., Coltro, W.K., Kubota, L.T., 2015. Lab Chip 15, 1651–1655.
Dieterich, K., 1902. US Patent, 691249, USA.
Dungchai, W., Chailapakul, O., Henry, C.S., 2010. Anal. Chim. Acta 674, 227–233.
Elizalde, E., Urteaga, R., Berli, C.L.A., 2015. Lab Chip 15, 2173–2180.
Elkins, H.B., Pagnotto, L.D., Smith, H.L., 1974. Am. Ind. Hyg. Assoc. J. 35, 559–565.
Fu, E., Lutz, B., Kauffman, P., Yager, P., 2010. Lab Chip 10, 918–920.
Fu, E., Ramsey, S.A., Kauffman, P., Lutz, B., Yager, P., 2011. Microfluid. Nanofluidics 10, 29–35.
Giokas, D.L., Tsogas, G.Z., Vlessidis, A.G., 2014. Anal. Chem. 86, 6202–6207.
Han, J.-W., Kim, B., Li, J., Meyyappan, M., 2012. J. Phys. Chem. C 116, 22094–22097.
Hossain, S.Z., Brennan, J.D., 2011. Anal. Chem. 83, 8772–8778.
Inman, B.A., Etienne, W., Rubin, R., Owusu, R.A., Oliveira, T.R., Rodriques, D.B., Maccarini, P.F., Stauffer, P.R., Mashal, A., Dewhirst, M.W., 2013. Int. J. Hyperther. 29, 206–210.
Jahanshahi-Anbuhi, S., Henry, A., Leung, V., Sicard, C., Pennings, K., Pelton, R., Brennan, J.D., Filipe, C.D., 2014. Lab Chip 14, 229–236.
Kaisti, M., 2017. Biosens. Bioelectron. 98, 437–448.
Kalish, B., Tan, M.K., Tsutsui, H., 2020. Micromachines 11, 773.
Korson, L., Drost-Hansen, W., Millero, F.J., 1969. J. Phys. Chem. 73, 34–39.
Kusy, R., Schafer, D., 1995. J. Mater. Sci. Mater. Med. 6, 385–389.
Li, H., Steckl, A.J., 2018. Anal. Chem. 91, 352–371.
Liu, Q., Xu, C., Liang, H., 2017. Talanta 175, 289–296.
Lowe, G.D., 2019. Clinical Blood Rheology: Volume I. CRC Press.
Martinez, A.W., Phillips, S.T., Butte, M.J., Whitesides, G.M., 2007. Angew. Chem. Int. Ed. 46, 1318–1320.
Ota, R., Yamada, K., Suzuki, K., Citterio, D., 2018. Analyst 143, 643–653.
Park, J., Park, J.-K., 2017. Sensor. Actuator. B Chem. 246, 1049–1055.
Rand, P.W., Lacombe, E., Hunt, H.E., Austin, W.H., 1964. J. Appl. Physiol. 19, 117–122.
Ratnarathorn, N., Chailapakul, O., Henry, C.S., Dungchai, W., 2012. Talanta 99, 552–557.
Renault, C., Li, X., Fosdick, S.E., Crooks, R.M., 2013. Anal. Chem. 85, 7976–7979.
Shen, Y., Modha, S., Tsutsui, H., Mulchandani, A., 2021. Biosens. Bioelectron. 171, 112721.
Shen, Y., Tran, T.-T., Modha, S., Tsutsui, H., Mulchandani, A., 2019. Biosens. Bioelectron. 130, 367–373.
Shin, J.-H., Lee, G.-J., Kim, W., Choi, S., 2016. Sensor. Actuator. B Chem. 230, 380–387.
Shin, J.H., Park, J., Kim, S.H., Park, J.-K., 2014. Biomicrofluidics 8, 054121.
Tlili, C., Cella, L.N., Myung, N.V., Shetty, V., Mulchandani, A., 2010. Analyst 135, 2637–2642.
Toley, B.J., McKenzie, B., Liang, T., Buser, J.R., Yager, P., Fu, E., 2013. Anal. Chem. 85, 11545–11552.
Verma, M.S., Tsaloglou, M.-N., Sisley, T., Christodouleas, D., Chen, A., Milette, J., Whitesides, G.M., 2018. Biosens. Bioelectron. 99, 77–84.
Villamizar, R.A., Maroto, A., Rius, F.X., Inza, I., Figueras, M.J., 2008. Biosens. Bioelectron. 24, 279–283.
Volk, A., Kähler, C.J., 2018. Exp. Fluid 59, 75.
Yamada, K., Kim, C.-T., Kim, J.-H., Chung, J.-H., Lee, H.G., Jun, S., 2014. PLoS One 9, e105767.
Yetisen, A.K., Akram, M.S., Lowe, C.R., 2013. Lab Chip 13, 2210–2251.